Symmetry breaking and circular photogalvanic effect in epitaxial $Cd_xHg_{1-x}Te$ films

S. Hubmann,[1] G. V. Budkin,[2] M. Otteneder,[1] D. But,[3] D. Sacré,[1] I. Yahniuk,[3] K. Diendorfer,[1] V. V. Bel'kov,[2] D. A. Kozlov,[4] N. N. Mikhailov,[4] S. A. Dvoretsky,[4] V. S. Varavin,[4] V. G. Remesnik,[4] S. A. Tarasenko,[2] W. Knap,[3,5] and S. D. Ganichev[1]

[1]*Terahertz Center, University of Regensburg, 93040 Regensburg, Germany*
[2]*Ioffe Institute, 194021 St. Petersburg, Russia*
[3]*CENTERA Laboratories, Institute of High Pressure Physics, Polish Academy of Sciences, PL-01-142 Warsaw, Poland*
[4]*Rzhanov Institute of Semiconductor Physics, 630090 Novosibirsk, Russia*
[5]*Laboratory Charles Coulomb, University of Montpellier and CNRS, Montpellier F-34095, France*

(Received 5 November 2019; revised manuscript received 4 February 2020; accepted 1 April 2020; published 28 April 2020)

We report on the observation of symmetry breaking and the circular photogalvanic effect in $Cd_xHg_{1-x}Te$ alloys. We demonstrate that irradiation of bulk epitaxial films with circularly polarized terahertz radiation leads to the circular photogalvanic effect (CPGE) yielding a photocurrent whose direction reverses upon switching the photon helicity. This effect is forbidden in bulk zinc-blende crystals by symmetry arguments; therefore, its observation indicates either the symmetry reduction of bulk material or that the photocurrent is excited in the topological surface states formed in a material with low cadmium concentration. We show that the bulk states play a crucial role because the CPGE was also clearly detected in samples with noninverted band structure. We suggest that strain is a reason for the symmetry reduction. We develop a theory of the CPGE showing that the photocurrent results from the quantum interference of different pathways contributing to the free-carrier absorption (Drude-like) of monochromatic radiation.

DOI: 10.1103/PhysRevMaterials.4.043607

I. INTRODUCTION

$Cd_xHg_{1-x}Te$ alloy, also known as MCT (mercury cadmium telluride), is one of the most leading materials used for sensitive and fast infrared detectors [1–7]. Wide bandgap tunability of these materials allows radiation detection in an extremely wide frequency range, spanning from near- to midinfrared wavelength. Furthermore, it has been used for the development of terahertz (THz) radiation detection; see, e.g., Refs. [8–12]. The introduction of the concept of topological insulators (TIs) [13–15] attracted great attention to novel aspects of $Cd_xHg_{1-x}Te$ compounds as well as low dimensional quantum heterostructures based on these materials. The reason for that is the inverted band structure of HgTe and $Cd_xHg_{1-x}Te$ with a cadmium fraction less than the critical value x_c, being $x_c \approx 0.17$ at 4.2 K [16–20]. The band inversion is a crucial condition for the formation of helical surface or edge states [14,15,20–25]. In comparison to other materials with a nontrivial band structure, CdHgTe-based compounds seem to be more promising due to their very high carrier mobility and feasibility to suppress effects from three-dimensional carriers in the sample volume. This is also supported by the well developed technological process originally motivated by the fabrication of detectors which has been adapted for the growth of TI materials on demand. The observation of Kane fermions in bulk $Cd_xHg_{1-x}Te$ crystals [17–19], quantum spin Hall effect [25–27], and helical edge photocurrents in CdHgTe/HgTe/CdHgTe quantum wells [28], as well as the demonstration of Dirac surface states in 3D TI made of strained HgTe [29–33], are some important achievements in the physics of topological insulators. In the case of bulk $Cd_xHg_{1-x}Te$ crystals the formation of helical surface states becomes possible due to the fact that the proper choice of the cadmium fraction in the alloy yields an inversion of the band ordering at $x = x_c$; see, e.g., Refs. [17,19,34]. Furthermore, in materials with low x the band structure can be changed from normal to inverted band ordering simply by a variation of the temperature, T [19]. Such x- and T-driven band inversions give rise to a large variety of novel physical concepts including the Veselago lenses [35], development of long wavelength lasers with suppression of the Auger processes [36,37], etc.

In all publications discussing the band structure, transport phenomena, optoelectronic effects, and magneto-optical properties of $Cd_xHg_{1-x}Te$ films the point group symmetry of the crystal is considered to be T_d. This follows from the crystallographic structure of the system. Here, investigating terahertz radiation induced photogalvanic currents in $Cd_xHg_{1-x}Te$ films with an inverted band structure we surprisingly observed a well pronounced circular photogalvanic effect (CPGE) [38,39], whose prerequisite is gyrotropy. Consequently, by symmetry arguments it is forbidden in the nongyrotropic T_d group.

Therefore, the CPGE observation indicates either (i) the symmetry reduction of the bulk material or (ii) excitation of the photocurrent in the topological surface states formed in the material with low cadmium concentration. We performed a careful study of terahertz radiation induced CPGE in bulk $Cd_xHg_{1-x}Te$ films with structure compositions similar to that in most of the previous studies of topological surface states in this material. We show that an attempt to ascribe the generation of the CPGE solely to the helical topological surface states fails, because pronounced CPGE is also detected in

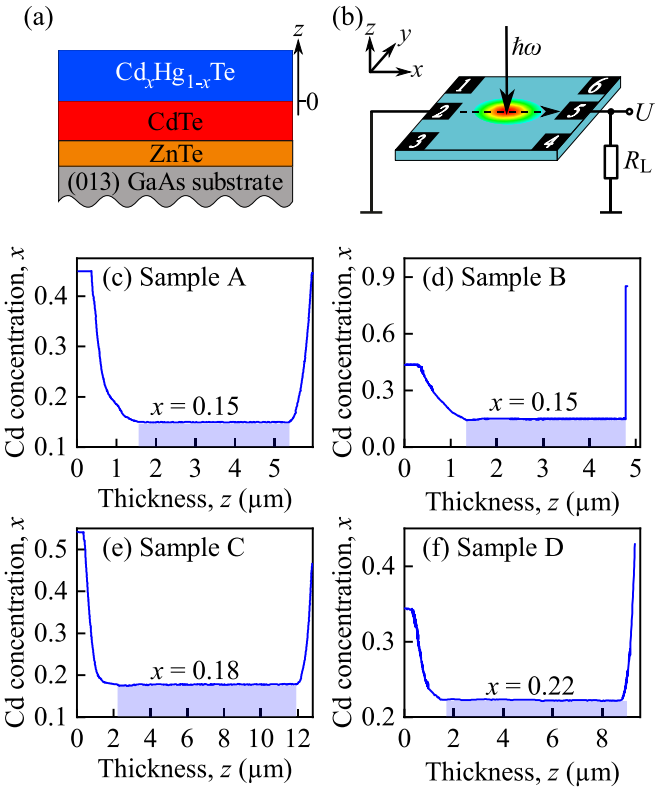

FIG. 1. (a) Sketch of the structure composition (not to scale). (b) Experimental setup. (c)–(f) Content of cadmium in the epitaxial layer as a function of the distance from the CdTe layer's top. The values of the Cd content x in the active $Cd_xHg_{1-x}Te$ layers for samples A–D are given in the plots.

crystals with x above the critical one, which, correspondingly, are characterized by a normal band ordering. To explain the origin of the observed CPGE, we suggest that the studied epitaxial films are strained and the actual symmetry of the crystal is reduced. In strained zinc-blende-type crystals, CPGE may emerge [40]. We develop a microscopic theory of the CPGE for the Drude-like indirect optical transitions in bulk crystals induced by terahertz radiation, which describes well the experimental findings. We show that the radiation helicity sensitive photocurrent stems from the interference of virtual transitions via the conduction and valence bands contributing to the real optical transitions.

II. SAMPLES AND METHODS

We studied $Cd_xHg_{1-x}Te$ layers with graded band gap layers at absorber boundaries grown by molecular beam epitaxy on semi-insulating (013)-oriented GaAs substrates. ZnTn (30 nm thick) and CdTe (6 μm thick) buffer layers [41] were fabricated on top of the GaAs substrates. A CdTe buffer layer with a thickness of more than 5 μm is needed to obtain the desired crystal quality for subsequent growth of CdHgTe [41–45].The structure composition is shown in Fig. 1(a). The samples were quadratically shaped with approximate dimensions of $5 \times 5\ mm^2$; see Fig. 1(b). Four samples with different profiles of the cadmium concentration x were prepared; see Figs. 1(c)–1(f). In three of these samples (A, C, and D) the active layers with constant x contents were sandwiched (surrounded) by regions with gradually growing cadmium concentration. In sample B, by contrast, the active layer was capped by 30 nm $Cd_{0.85}Hg_{0.15}Te$. Note that due to the Fermi level position free carriers are located in the active layer and in the films with $x < x_c$ in the topological surface states. The samples were supplied with several indium-soldered contacts bonded to a chip holder; see Fig. 1(b).

As a radiation source for the photocurrent measurements two types of molecular gas THz lasers were used. On the one hand, a continuous wave (cw) laser with a power P of up to 60 mW [46]; on the other hand, a pulsed laser with a pulse duration of about 100 ns, a repetition rate of 1 Hz, and a peak power P of up to 60 kW [47–49]. The lasers emitted frequency lines in the range between 0.6 and 2.6 THz. The corresponding photon energies $\hbar\omega$ from 2.5 to 10.8 meV are smaller than the band gap E_g, being in the order of 50 to 200 meV in studied samples. Thus THz radiation is absorbed via free-carrier (Drude-like) absorption. The nearly Gaussian-shaped beam, controlled by a pyroelectric camera [50], was focused onto the sample using a parabolic mirror. The beam spot diameter varied, depending on the radiation frequency, from 1.5 to 3 mm. The initially linearly polarized radiation was modified applying lambda-quarter plates made from crystal quartz. The rotation of these plates by the angle φ with respect to the initial laser polarization plane resulted in the controllable variation of the radiation polarization state. By that the degree of circular polarization $P_{\rm circ}$ was changed according to

$$P_{\rm circ} = \frac{I^{\sigma^+} - I^{\sigma^-}}{I^{\sigma^+} + I^{\sigma^-}} = \sin(2\varphi), \qquad (1)$$

where $I^{\sigma^+}(I^{\sigma^-})$ is the intensity of the right- (left-) handed circularly polarized radiation part. The Stokes parameters defining the degrees of linear polarization were varied according to [51]

$$P_{\rm L1} = \frac{\cos(4\varphi)+1}{2}, \quad P_{\rm L2} = \frac{\sin(4\varphi)}{2}. \qquad (2)$$

THz radiation was applied at normal incidence. The photocurrent was measured as a voltage drop across a load resistor, see Fig. 1(b), or as the voltage drop over the sample itself. The measurements were carried out in an optical cryostat which allowed us to access a temperature range from liquid helium to room temperature.

III. RESULTS

The circular photocurrent was first observed at liquid helium temperature in samples A and B with $x = 0.15$ being characterized by the inverted band structure. The characteristic feature of the circular photocurrent is that it is excited by circularly polarized radiation and has opposite sign for opposite helicities. Figure 2 shows the data obtained at normally incident radiation of low power cw radiation with frequencies 1.63 and 2.54 THz. The overall polarization dependences can be well fitted by

$$J = J_c \sin(2\varphi) + J_0 + J_{\rm L1}\frac{\cos(4\varphi)+1}{2} + J_{\rm L2}\frac{\sin(4\varphi)}{2}. \qquad (3)$$

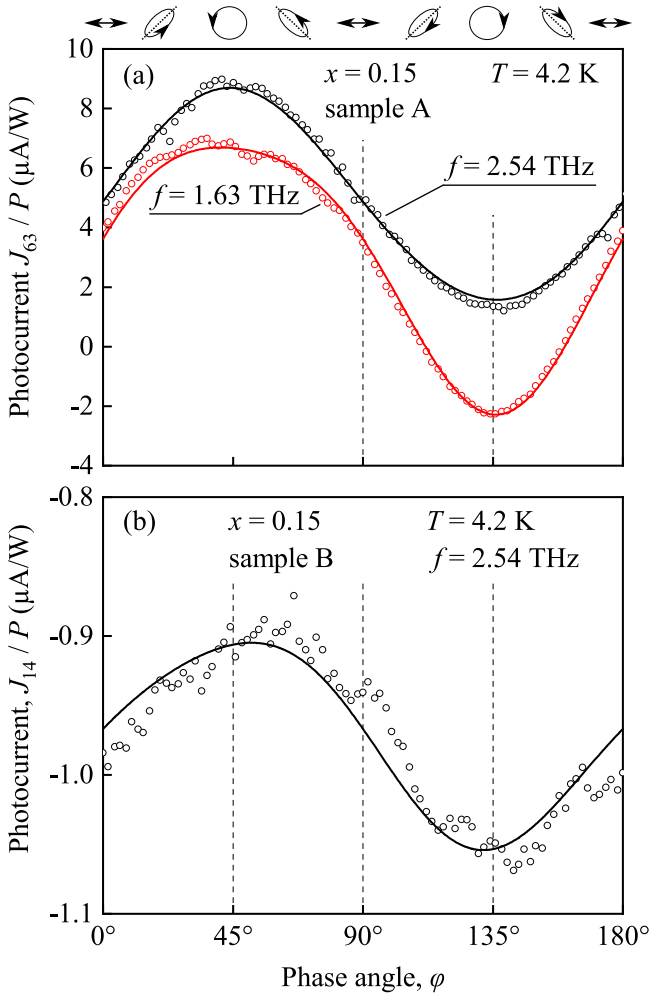

FIG. 2. Photocurrents between contacts 6 and 3 (a) and 1 and 4 (b) [see Fig. 1(b)] as a function of radiation helicity measured at liquid helium temperature in $Cd_xHg_{1-x}Te$ crystals with a cadmium concentration $x \approx 0.15$. The photocurrent was excited by THz radiation from a low power cw laser ($P \approx 47$ mW) operating at frequencies 1.63 and 2.54 THz. Solid curves show fits after Eq. (3). The corresponding fitting parameters are shown in Table II. Along the top the polarization ellipses corresponding to key phase angles φ are sketched.

In both samples the total photocurrent is dominated by the circular photocurrent described by the first term in Eq. (3) proportional to the coefficient, J_c, and the polarization independent offset, J_0. Contributions proportional to the degrees of linear polarization, while being present, are substantially smaller. Generally, in noncentrosymmetric bulk $Cd_xHg_{1-x}Te$ crystals polarization independent photocurrents as well as those proportional to the degree of linear polarization can stem from linear photogalvanic or photon drag effects [38,39,52]. These effects are well known for other noncentrosymmetric materials and are out of the scope of our paper. By contrast, in such crystals, both the circular photogalvanic and the circular photon drag effects are forbidden by symmetry arguments; see Secs. IV A and IV C. Therefore, below we focus on the origin and properties of the circular photocurrent.

Samples A and B at liquid helium temperature have a Cd concentration in the active layer lower than the critical one and, therefore, are characterized by an inverted band ordering. The latter results in the formation of topological surface states. These states, at least for samples with an abrupt increase of the cadmium concentration x, like in the top layer of sample B, are two-dimensional and, therefore, are characterized by reduced symmetry. Consequently, in such states the circular photocurrent becomes possible. To prove that formation of the surface states is an unambiguous requirement for the generation of the circular photocurrent in the bulk $Cd_xHg_{1-x}Te$ crystals we carried out measurements at liquid helium temperature in samples with normal band ordering (sample D, active layer $x = 0.22$) and with almost linear dispersion (sample C, active layer with cadmium concentration $x = 0.18$ being close to the critical one). Figure 3 shows the data obtained applying normally incident radiation of a cw laser operating at frequencies 0.69, 1.63, and 2.54 THz. In both cases the photocurrent can be well fitted by Eq. (3), surprisingly, with substantial contribution of the circular photocurrent. These results already rule out band inversion and topological states formation as a prerequisite of the circular photocurrent in bulk $Cd_xHg_{1-x}Te$ crystals. Moreover, applying the radiation of high power pulsed lasers, which increases the sensitivity of the method, we observed that the circular photocurrent can clearly be detected even at room temperature. This is shown in Fig. 4 for samples A and C with $x \approx 0.15$ and $x \approx 0.18$. Previous studies of $Cd_xHg_{1-x}Te$ crystals demonstrated that at room temperature all our samples are characterized by a normal band order and no topological states are present.

Summarizing the experimental part, our experiments provide clear evidence for the generation of the circular photocurrent in bulk $Cd_xHg_{1-x}Te$ crystals with both inverted and normal band orderings, as well as for samples with critical cadmium concentration characterized by an almost linear energy dispersion. The fact that the circular photocurrent is clearly detected for samples with x larger than the critical one demonstrates that the circular photocurrent generation is not limited to the films with topological surface states.

IV. THEORY AND DISCUSSION

As addressed above, the circular photocurrent may arise from the circular photogalvanic and the circular photon drag effects. Below we present a symmetry analysis of both effects (Secs. IV A and IV C) and a microscopic theory of the circular photogalvanic effect (Sec. IV B), as well as a comparison of the magnitude of these effects (Sec. IV C). The latter shows that the photocurrent is dominated by the CPGE; therefore, we focus on this effect in the analysis below.

A. Symmetry analysis of the CPGE

Bulk $Cd_xHg_{1-x}Te$ has nominally zinc-blende crystal structure which is described by the T_d point group. Despite the fact that the group lacks the center of space inversion, it is nongyrotropic and does not support CPGE [38]. However, if the spatial symmetry of the crystal is reduced further, CPGE may emerge. The most likely origin of the symmetry reduction

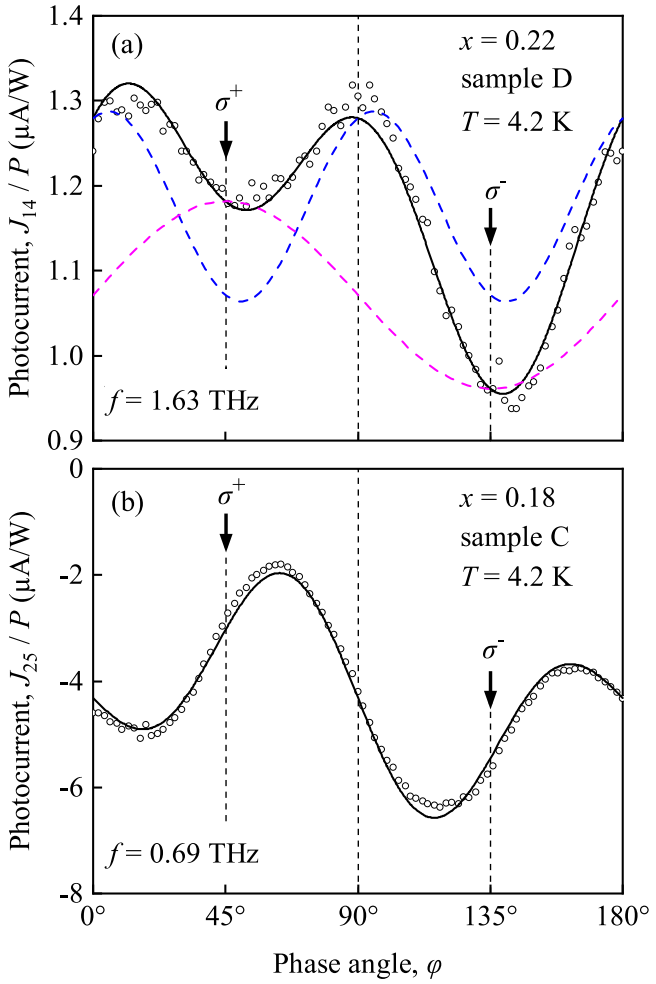

FIG. 3. Photocurrents between contacts 1 and 4 (a) and 2 and 5 (b) [see Fig. 1(b)] as a function of radiation helicity measured at liquid helium temperature in $Cd_xHg_{1-x}Te$ crystals with active layer cadmium concentrations $x = 0.22$ (sample D, $f = 1.63$ THz) and 0.18 (sample C, $f = 0.69$ THz). The photocurrent was excited by THz radiation from a low power cw laser ($P \approx 20$ mW for $f = 0.69$ THz; $P \approx 56$ mW for $f = 1.63$ THz). The solid curves show fits according to Eq. (3). The corresponding fitting parameters are shown in Table II. The magenta dashed curve in panel (a) shows the corresponding contribution of the circular photocurrent J_c and the blue dashed line the one proportional to the degree of linear polarization P_{L2}. Note that both dashed lines are shifted by an offset of J_0.

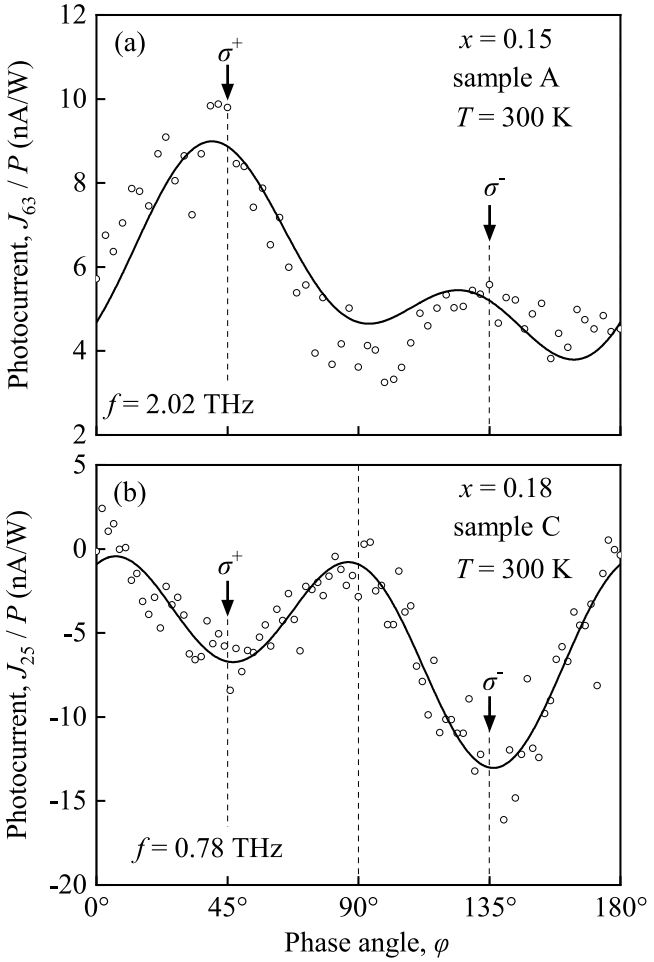

FIG. 4. Photocurrents between contacts 6 and 3 (a) and 2 and 5 (b) [see Fig. 1(b)] as a function of radiation helicity measured at room temperature in $Cd_xHg_{1-x}Te$ crystals with an active layer cadmium concentration $x = 0.15$ (sample A, $f = 2.02$ THz) and 0.18 (sample C, $f = 0.78$ THz). The photocurrent was excited by THz radiation from a high power pulsed laser ($P \approx 4$ kW). The solid curves show fits according to Eq. (3). The corresponding fitting parameters are shown in Table II.

in our samples is strain stemming, e.g., from lattice mismatch at the $Cd_xHg_{1-x}Te$ film interfaces [53].

In strained zinc-blende crystals, CPGE can occur [40]. To first order in strain, the dependence of the CPGE current density $\boldsymbol{j}$ on the static strain tensor $\boldsymbol{u}$ is described by

$$\begin{aligned} j_{x'} &= [\chi_1(u_{y'y'} - u_{z'z'})\hat{e}_{x'} + \chi_2(u_{x'y'}\hat{e}_{y'} - u_{x'z'}\hat{e}_{z'})]IP_{\text{circ}}, \\ j_{y'} &= [\chi_1(u_{z'z'} - u_{x'x'})\hat{e}_{y'} + \chi_2(u_{y'z'}\hat{e}_{z'} - u_{x'y'}\hat{e}_{x'})]IP_{\text{circ}}, \\ j_{z'} &= [\chi_1(u_{x'x'} - u_{y'y'})\hat{e}_{z'} + \chi_2(u_{x'z'}\hat{e}_{x'} - u_{y'z'}\hat{e}_{y'})]IP_{\text{circ}}, \end{aligned} \quad (4)$$

where $\hat{\boldsymbol{e}} = \boldsymbol{q}/q$ is the unit vector pointing along the photon wave vector $\boldsymbol{q}$, I is the local intensity of radiation, and $x' \parallel [100]$, $y' \parallel [010]$, and $z' \parallel [001]$ are the cubic axes.

The parameters χ_1 and χ_2 are linearly independent and describe the contributions to the photocurrent caused by normal and shear strain, respectively [40]. The CPGE current vanishes in the case of hydrostatic strain that does not disturb the crystal symmetry. Phenomenological Eqs. (4) can be readily constructed using the theory of group representations. In (013)-grown structures experimentally studied in our work, the tensor of strain induced by the lattice mismatch has four nonzero components u_{xx}, u_{yy}, u_{zz}, and u_{yz} in the coordinate frame $x \parallel [100]$, $y \parallel [03\bar{1}]$, and $z \parallel [013]$ relevant to the structure orientation. Typically, the components u_{xx} and u_{yy} at the interfaces are determined by the lattice mismatch between the film and the buffer layer and are equal to each other. The other components, u_{zz} and u_{yz}, can be found by minimizing the elastic energy; see, e.g., Ref. [33].

In the experiment on (013)-grown samples described above, we study the photocurrent excited by normally incident

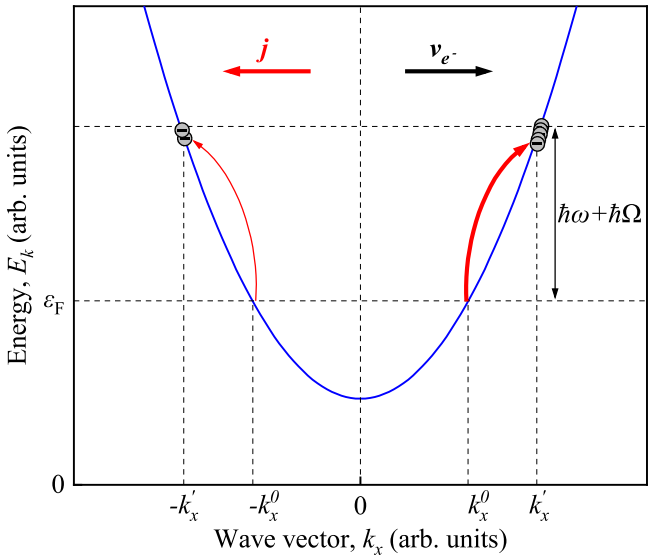

FIG. 5. Photocurrent generation via Drude-like indirect optical transitions. The radiation with frequency ω is absorbed with simultaneous absorption or emission of a phonon with frequency Ω. For circularly polarized radiation, the transitions are asymmetric in the $\boldsymbol{k}$ space (thin and thick arrows) resulting in a photocurrent. The asymmetry comes from interference of different pathways contributing to the transitions; see Fig. 6.

radiation. For this geometry, $\hat{\boldsymbol{e}} \parallel z$ and Eqs. (4) take the form

$$j_y = \left[(\chi_1+\chi_2)(u_{zz}-u_{yy})\frac{\sin 2\phi}{2} + \chi_2 u_{yz}\cos 2\phi\right] I P_{\rm circ},$$
$$j_z = -\chi_1 u_{yz}\sin 2\phi\, I P_{\rm circ}, \tag{5}$$

where ϕ is the angle between [001] and [013], $\phi = \arctan(1/3)$. A substantial photocurrent excited at normal incidence and sensitive to the degree of circular polarization $P_{\rm circ}$ has been detected in all samples for all frequencies and temperatures used; see Figs. 2–4. This photocurrent corresponds to the in-plane component of photocurrent j_y in Eq. (5). Note that the geometry of the samples allows us to measure only the in-plane component of the current.

B. Microscopic theory of the CPGE

Now we turn to the microscopic mechanism of the photocurrent generation. We consider $Cd_xHg_{1-x}Te$ with the content of Hg below the critical value of the transition to a 3D topological insulator. The samples have the conventional band structure with the Γ_6 conduction band and the Γ_8 valence band. The band gap is larger than the photon energy of THz radiation and free carriers are present in the sample. Therefore, as addressed above, the radiation is absorbed via indirect optical transitions (Drude-like) in the conduction band; see Fig. 5. These transitions are assisted by the scattering of electrons by phonons or static defects of the structure to simultaneously satisfy the laws of energy and quasimomentum conservation. Indirect optical transitions are described by the second-order perturbation theory involving virtual processes via intermediate states. The matrix element of the real transition from the initial state $i = (\boldsymbol{k}, s)$, where $\boldsymbol{k}$ is the wave vector and s is the spin index, to the final state $f = (\boldsymbol{k}', s')$ is given by the sum of the compound matrix elements of the virtual transitions via all possible intermediate states j,

$$M_{fi} = \sum_j \left(\frac{V_{fj}R_{ji}}{E_i - E_j} + \frac{R_{fj}V_{ji}}{E_i - E_j}\right), \tag{6}$$

where V_{fj} and R_{ji} are the matrix elements of the electron scattering and electron-phonon interaction, respectively, and E_j is the total energy of the system in the j state.

The main contribution to radiation absorption comes from the virtual transitions with intermediate states in the conduction band, Fig. 6. There are two types of such processes: the processes where electron-photon interaction is followed by electron scattering [shown in Fig. 6(a)] and the processes with the opposite order [shown in Fig. 6(b)]. The virtual transitions via the conduction-band states describe well the Drude absorption. However, they are not sensitive to the

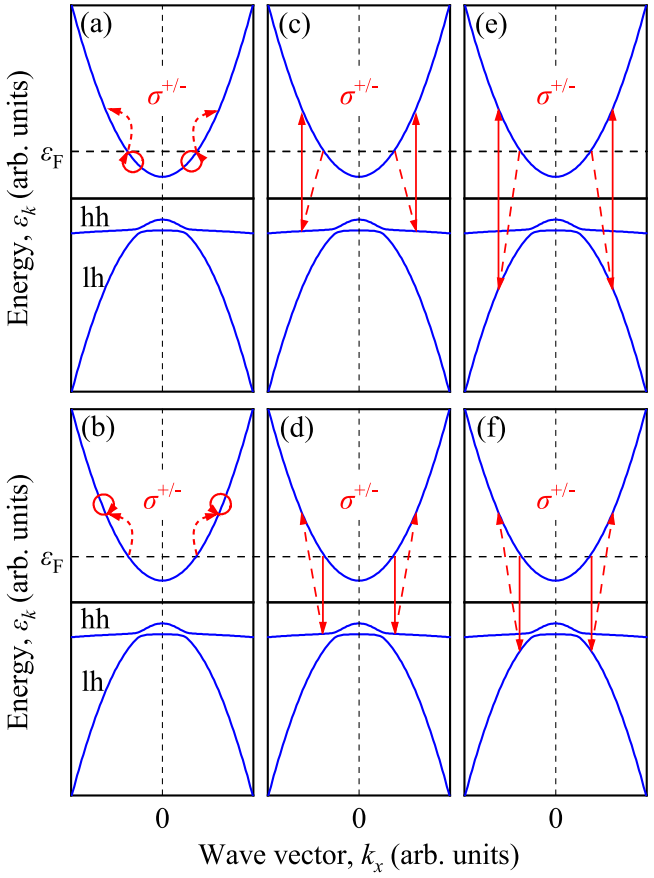

FIG. 6. Panels (a) and (b): virtual intraband optical transitions with intermediate states in the conduction band. Red circles and red dashed arrows denote electron-photon interaction and electron scattering, respectively. Panel (a) corresponds to the process when photon absorption is followed by electron scattering, while panel (b) sketches the process in the opposite order. Panels (c)–(f): virtual intraband optical transitions with intermediate states in the heavy-hole and light-hole subbands. Red solid and red dashed arrows denote interband electron-photon interaction and electron scattering, respectively. The mixing of heavy-hole and light-hole states by static strain, essential for the emergence of the CPGE in zinc-blende crystals, is shown as the distortion of the valence-band spectrum.

circular polarization of the radiation and do not introduce asymmetry in the electron distribution in the $\boldsymbol{k}$ space.

To obtain the photocurrent, one should also take into account the virtual transitions with intermediate states in the valence band [54]. Figures 6(c)–6(f) sketch four possible processes of such type via the heavy-hole and the light-hole bands. Due to the selection rules for interband optical transitions, these processes are sensitive to the radiation helicity [55]. Moreover, their contributions can be quite large because the band gap in CdHgTe samples, and correspondingly the denominator in Eq. (6), is small.

The probability of the real transitions $(\boldsymbol{k}, s) \to (\boldsymbol{k}', s')$ is determined by the squared modulus of the matrix element

$$|M_{\boldsymbol{k}'s',\boldsymbol{k}s}|^2 = \left|M^{(c)}_{\boldsymbol{k}'s',\boldsymbol{k}s} + M^{(v)}_{\boldsymbol{k}'s',\boldsymbol{k}s}\right|^2, \tag{7}$$

where $M^{(n)}_{\boldsymbol{k}'s',\boldsymbol{k}s}$ are the matrix elements of the virtual transitions via the n band. It contains the interference term $2\,\mathrm{Re}[M^{(c)*}_{\boldsymbol{k}'s',\boldsymbol{k}s} M^{(v)}_{\boldsymbol{k}'s',\boldsymbol{k}s}]$. The term does not vanish in noncentrosymmetric crystals and is responsible for the circular photogalvanic effect [54].

The circular photocurrent emerges only in strained crystals. Therefore, in the calculation of the matrix elements of the virtual transitions we also take into account the mixing of the states by the static strain. Otherwise, the photocurrent vanishes in agreement with the symmetry analysis presented above. The strain-induced mixing of the heavy-hole and light-hole states is schematically shown in Fig. 6 as a distortion of the valence-band spectrum.

To summarize, the microscopic model takes into account two ingredients essential for the CPGE: (i) the lack of space inversion center in the crystal which enables the interference of the optical transition pathways via the conduction and valence bands and (ii) the strain-induced mixing of the states.

We calculate the photocurrent considering the static strain of the crystal and the electron scattering by acoustic phonons. In the studied CdHgTe films, the band gap is much smaller than both the split-off energy and the energy of higher conduction band. Consequently, the bands involved in optical transitions are the conduction, heavy-hole, and light-hole bands. Accordingly, the electron dispersion and states are described in the six-band ($\Gamma_6, \pm 1/2$, $\Gamma_8, \pm 1/2$, and $\Gamma_8, \pm 3/2$) Kane Hamiltonian relevant for narrow-gap semiconductors with zinc-blende structure [16]. In the basis of the Γ_6 and Γ_8 states, the Kane Hamiltonian has the form [56]

$$H = \begin{pmatrix} 0_2 & H_{\mathrm{cv}} \\ H^{\dagger}_{\mathrm{cv}} & -E_g I_4 \end{pmatrix}, \tag{8}$$

where 0_2 is the 2×2 zero matrix, I_4 is the 4×4 identity matrix,

$$H^{\dagger}_{\mathrm{cv}} = P \begin{pmatrix} -\dfrac{k_{x'} - ik_{y'}}{\sqrt{2}} & 0 \\ \sqrt{\dfrac{2}{3}} k_{z'} & -\dfrac{k_{x'} - ik_{y'}}{\sqrt{6}} \\ \dfrac{k_{x'} + ik_{y'}}{\sqrt{6}} & \sqrt{\dfrac{2}{3}} k_{z'} \\ 0 & \dfrac{k_{x'} + ik_{y'}}{\sqrt{2}} \end{pmatrix}, \tag{9}$$

and P is the Kane parameter. The Hamiltonian (8) describes six eigenstates: the conduction-band states $|e, \boldsymbol{k}, \pm 1/2\rangle$ with the dispersion $\varepsilon_{c,k} = \hbar^2 k^2/(2m^*)$, the states in the light-hole subband $|lh, \boldsymbol{k}, \pm 1/2\rangle$ with the dispersion $\varepsilon_{lh,k} = -E_g - \hbar^2 k^2/(2m^*)$, and the dispersionless states in the heavy-hole subband $|hh, \boldsymbol{k}, \pm 3/2\rangle$ with the energy $\varepsilon_{hh} = -E_g$. Here, $m^* = 3\hbar^2 E_g/(4P^2)$ is the effective mass. The Hamiltonian of electron-photon interaction is given by

$$R = -\frac{e}{\hbar c} \boldsymbol{A} \cdot \boldsymbol{\nabla}_k H, \tag{10}$$

where e is the electron charge, c is the speed of light, $\boldsymbol{A}$ is the vector potential of the electromagnetic field related to the radiation intensity I by $I = A^2 \omega^2 n_\omega/(2\pi c)$, and n_ω is the refractive index of the crystal. The influence of deformation on the six-band Hamiltonian is described in detail in [56,57]. The strain Hamiltonian is given by

$$V = \begin{pmatrix} \Xi_c\ \mathrm{Tr}\,(\boldsymbol{\epsilon})\, I_2 & V_{\mathrm{cv}} \\ V^{\dagger}_{\mathrm{cv}} & V_{\mathrm{BP}} \end{pmatrix}, \tag{11}$$

where Ξ_c in the conduction-band deformation potential, $\boldsymbol{\epsilon}$ is the strain tensor, V_{BP} is the Bir-Pikus Hamiltonian which, in the spherical approximation, has the form [56]

$$V_{\mathrm{BP}} = \left(a + \frac{5}{4} b\right) I_4\, \mathrm{Tr}(\boldsymbol{\epsilon}) - b \sum_{\alpha\beta} J_\alpha J_\beta\, \epsilon_{\alpha\beta}, \tag{12}$$

a and b are the valence-band deformation potentials, J_α are the matrices of the angular momentum 3/2, and V_{cv} is the part describing the strain-induced coupling of the Γ_6 and Γ_8 states in zinc-blende crystals [55,57],

$$V^{\dagger}_{\mathrm{cv}} = \Xi_{\mathrm{cv}} \begin{pmatrix} -\dfrac{i\epsilon_{y'z'} + \epsilon_{x'z'}}{\sqrt{2}} & 0 \\ i\sqrt{\dfrac{2}{3}} \epsilon_{x'y'} & -\dfrac{i\epsilon_{y'z'} + \epsilon_{x'z'}}{\sqrt{6}} \\ \dfrac{i\epsilon_{y'z'} - \epsilon_{x'z'}}{\sqrt{6}} & i\sqrt{\dfrac{2}{3}} \epsilon_{x'y'} \\ 0 & \dfrac{i\epsilon_{y'z'} - \epsilon_{x'z'}}{\sqrt{2}} \end{pmatrix}, \tag{13}$$

and Ξ_{cv} is the interband deformation potential, which vanishes in centrosymmetric crystals. The Hamiltonian (11) is used to calculate both the mixing of the states by the static strain $\boldsymbol{u}$ and the electron scattering by longitudinal acoustic (LA) phonons. The tensor of strain produced by the LA phonons is given by

$$\epsilon_{\alpha\beta} = i \sum_{\boldsymbol{q}} \frac{q_\alpha q_\beta}{q^2} \sqrt{\frac{\hbar q^2}{2\rho\, \Omega_q}} \left(e^{i\boldsymbol{q}\cdot\boldsymbol{r}} a_{\boldsymbol{q}} - e^{-i\boldsymbol{q}\cdot\boldsymbol{r}} a^{\dagger}_{\boldsymbol{q}}\right), \tag{14}$$

where $\boldsymbol{q}$ is the phonon wave vector, ρ is the crystal density, $\Omega_q = c_s q$ is the photon frequency, c_s is the speed of longitudinal sound, and $a_{\boldsymbol{q}}$ and $a^{\dagger}_{\boldsymbol{q}}$ are the operators of phonon annihilation and creation, respectively. We assume that the photon frequency ω considerably exceeds both the frequency of phonons involved in scattering $\Omega_{|\boldsymbol{k}'-\boldsymbol{k}|}$ and the scattering rate τ^{-1}, and that the phonon occupation numbers are large, i.e., $k_B T/(\hbar\Omega_{|\boldsymbol{k}'-\boldsymbol{k}|}) \gg 1$, where T is the temperature. To the first order in the wave vector, the matrix elements of the virtual

transitions via the conduction band with the absorption of a photon and the simultaneous emission (+) or absorption (−) of a LA phonon have the form

$$M^{(c,\pm)}_{\boldsymbol{k}'s',\boldsymbol{k}s} = \pm i\,\frac{e\,m^*\,\Xi_c\,\boldsymbol{A}(\boldsymbol{k}-\boldsymbol{k}')}{c\,\omega}\sqrt{\frac{k_BT}{2\,\rho\,c_s^2}}\;\delta_{s',s}. \tag{15}$$

In calculating the matrix elements of the virtual transitions via the valence band we take into account the mixing of the heavy hole and light hole states by the static strain. The corresponding contribution to $M^{(v)}_{\boldsymbol{k}'s',\boldsymbol{k}s}$ proportional to the static strain can be obtained by the third-order perturbation theory and is given by

$$M^{(v,\pm)}_{\boldsymbol{k}'s',\boldsymbol{k}s} = \sum_{m,n}\left\{\frac{V^{(\pm)}_{\boldsymbol{k}'s',\boldsymbol{k}m}U_{\boldsymbol{k}m,\boldsymbol{k}n}R_{\boldsymbol{k}n,\boldsymbol{k}s}}{(\varepsilon_{ck}+\hbar\omega-\varepsilon_{mk})(\varepsilon_{ck}+\hbar\omega-\varepsilon_{nk})}+\frac{R_{\boldsymbol{k}'s',\boldsymbol{k}'m}U_{\boldsymbol{k}'m,\boldsymbol{k}'n}V^{(\pm)}_{\boldsymbol{k}'n,\boldsymbol{k}s}}{(\varepsilon_{ck}-\varepsilon_{mk'})(\varepsilon_{ck}-\varepsilon_{nk'})}+\frac{V^{(\pm)}_{\boldsymbol{k}'s',\boldsymbol{k}m}R_{\boldsymbol{k}m,\boldsymbol{k}n}U_{\boldsymbol{k}n,\boldsymbol{k}s}}{(\varepsilon_{ck}+\hbar\omega-\varepsilon_{mk})(\varepsilon_{ck}-\varepsilon_{nk})}\right.$$
$$\left.+\frac{U_{\boldsymbol{k}'s,\boldsymbol{k}'m}V^{(\pm)}_{\boldsymbol{k}'m,\boldsymbol{k}n}R_{\boldsymbol{k}n,\boldsymbol{k}s}}{(\varepsilon_{ck}+\hbar\omega-\varepsilon'_{mk})(\varepsilon_{ck}+\hbar\omega-\varepsilon_{nk})}+\frac{U_{\boldsymbol{k}'s,\boldsymbol{k}'m}R_{\boldsymbol{k}'m,\boldsymbol{k}'n}V^{(\pm)}_{\boldsymbol{k}'n,\boldsymbol{k}cs}}{(\varepsilon_{ck}+\hbar\omega-\varepsilon_{nk'})(\varepsilon_{ck}-\varepsilon_{mk'})}+\frac{R_{\boldsymbol{k}'s,\boldsymbol{k}'m}V^{(\pm)}_{\boldsymbol{k}'m,\boldsymbol{k}n}U_{\boldsymbol{k}n,\boldsymbol{k}s}}{(\varepsilon_{ck}-\varepsilon_{mk'})(\varepsilon_{ck}-\varepsilon_{nk})}\right\}, \tag{16}$$

where the indexes m and n run over the valence subbands. The matrix elements of electron scattering with the emission or absorption of a LA phonon $V^{(\pm)}_{\boldsymbol{k}'s',\boldsymbol{k}m}$ and the matrix elements of heavy-hole–light-hole mixing by the static strain $U_{\boldsymbol{k}m,\boldsymbol{k}n}$ are calculated using the strain Hamiltonian (11). The exact analytical expression for $M^{(v)}_{\boldsymbol{k}'s',\boldsymbol{k}s}$ is too cumbersome to be printed. An estimation capturing the dependence on the band-structure parameters and deformation potentials is the following: $M^{(v)}_{\boldsymbol{k}'s,\boldsymbol{k}s}\sim(e\,\omega\,u\,b\,A\,P\,\Xi_{cv}/c\,E_g^3)\sqrt{k_BT/\rho\,c_s^2}$.

The photocurrent in the relaxation time approximation is given by the standard expression

$$\boldsymbol{j} = e\tau\sum_{\boldsymbol{k}\boldsymbol{k}'s,\pm}\frac{2\pi}{\hbar}\left|M^{(c,\pm)}_{\boldsymbol{k}'s,\boldsymbol{k}s}+M^{(v,\pm)}_{\boldsymbol{k}'s,\boldsymbol{k}s}\right|^2(\boldsymbol{v}_{\boldsymbol{k}'}-\boldsymbol{v}_{\boldsymbol{k}})[f(\varepsilon_{ck})$$
$$-f(\varepsilon_{ck'})]\delta(\varepsilon_{ck'}-\varepsilon_{ck}-\hbar\omega), \tag{17}$$

where τ is the momentum relaxation time, $\boldsymbol{v}=\hbar\boldsymbol{k}/m^*$ is the electron velocity, and $f(\varepsilon_{ck})$ is the equilibrium Fermi-Dirac distribution function.

Labor-consuming calculation of Eq. (17) with the matrix elements (15) and (16) yields the CPGE current (4) with the coefficients

$$\chi_1 = -\frac{512\pi^2}{315}\frac{e^3\tau}{\hbar^2 c\,n_\omega}\frac{k_BT}{\rho\,c_s^2}\frac{\Xi_{\rm cv}\,\Xi_{\rm c}}{(\hbar\omega)^2}\frac{b}{}\frac{P^5}{E_g^5}\sum_{\boldsymbol{k}\boldsymbol{k}'}[f(\varepsilon_{ck})-f(\varepsilon_{ck'})]$$
$$\times(k'^2+k^2)\,\delta(\varepsilon_{ck'}-\varepsilon_{ck}-\hbar\omega) \tag{18}$$

and $\chi_2=-(5/3)\chi_1$. Now using Eq. (5) one can already obtain the equation for the in-plane photocurrent which describes well all major experimental findings. To proceed further, we assume that the momentum relaxation of electrons is also determined by the electron-phonon interaction. For quasielastic scattering by LA phonons, the momentum relaxation time depends on energy and has the form

$$\frac{1}{\tau(\varepsilon_k)} = \frac{m^*}{\pi\hbar^3}\frac{k_BT\,\Xi_c^2}{\rho\,c_s^2}\sqrt{\frac{2m^*\varepsilon_k}{\hbar^2}}. \tag{19}$$

The relaxation time of the average electron velocity in the model of the drifting electron gas is given by

$$\frac{1}{\tau} = \sum_{\boldsymbol{k}}\frac{\varepsilon_k}{\tau(\varepsilon_k)}\frac{df(\varepsilon_k)}{d\varepsilon_k}\Bigg/\sum_{\boldsymbol{k}}\varepsilon_k\frac{df(\varepsilon_k)}{d\varepsilon_k}, \tag{20}$$

which gives

$$\frac{1}{\tau} = \frac{4m^*}{3\pi\hbar^3}\frac{k_BT\,\Xi_c^2}{\rho\,c_s^2}\,\bar{k}, \tag{21}$$

where

$$\bar{k} = \sum_{\boldsymbol{k}}|\boldsymbol{k}|f(\varepsilon_k)\Bigg/\sum_{\boldsymbol{k}}f(\varepsilon_k) \tag{22}$$

is the mean value of $|\boldsymbol{k}|$. Taking into account Eq. (21) and $m^*=3\hbar^2E_g/(4P^2)$, we can rewrite Eq. (18) in the form

$$\chi_1 = -\frac{18}{35\pi}\frac{e^3}{\hbar^3\omega^2\,c\,n_\omega\,\bar{k}}\frac{\Xi_{\rm cv}}{\Xi_{\rm c}}\frac{b}{E_g^2P}\int d\varepsilon\sqrt{\varepsilon(\varepsilon+\hbar\omega)}$$
$$\times(2\varepsilon+\hbar\omega)[f(\varepsilon)-f(\varepsilon+\hbar\omega)]. \tag{23}$$

In the case when the photon energy $\hbar\omega$ is much less than the mean electron energy $\bar{\varepsilon}$, Eq. (23) takes the form

$$\chi_1 = -\frac{64\pi}{35}\frac{e^3N_eb}{\hbar^2\omega\,c\,n_\omega}\frac{\Xi_{\rm cv}}{\Xi_{\rm c}}\frac{P^3}{E_g^4}, \tag{24}$$

where $N_e=2\sum_{\boldsymbol{k}}f_{\varepsilon_{\boldsymbol{k}}}$ is the electron density.

Finally, the in-plane photocurrent induced at normal incidence of radiation in (013)-oriented films is given by

$$j_y = \frac{64\pi}{21}\frac{e^3N_eb}{\hbar^2\omega c n_\omega}\frac{\Xi_{\rm cv}}{\Xi_{\rm c}}\frac{P^3}{E_g^4}$$
$$\times\left[\frac{2}{5}(u_{zz}-u_{yy})\frac{\sin 2\phi}{2}-u_{yz}\cos 2\phi\right]IP_{\rm circ}. \tag{25}$$

The limits of applicability of Eq. (25) are the frequency range $\hbar/\tau\ll\hbar\omega\ll\bar{\varepsilon},E_g$. This equation describes the observed polarization dependence of the photocurrent and its almost linear increase with the frequency decrease, as well as the drastic increase of the photocurrent magnitude by cooling the sample from room to liquid helium temperature. Indeed, the proportionality of the photocurrent J_c to the radiation helicity $P_{\rm circ}$ has already been addressed above and is clearly seen in Figs. 1–4 obtained for 4.2 and 300 K. The inset in Fig. 7 presenting the circular photocurrent as a function of the radiation frequency shows that it varies after $J_c\propto 1/\omega$, which agrees with Eq. (25) [58].

Results obtained for samples with different Cd contents x and temperatures are characterized by substantially different

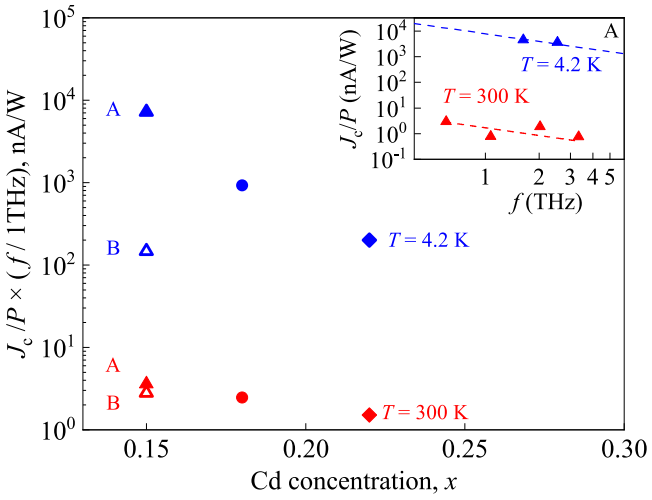

FIG. 7. Dependence of the circular photocurrent contribution normalized to radiation frequency on the cadmium concentration x for temperatures $T = 4.2$ K (blue symbols) and $T = 300$ K (red symbols). The inset shows the dependence of the circular photocurrent on the frequency for sample A at temperatures $T = 4.2$ K (blue symbols) and $T = 300$ K (red symbols). Dashed lines in the inset indicate a fit of J_c/P according to $J_c/P \propto 1/f$.

energy gaps. According to Eq. (25) the latter should strongly affect the circular photocurrent magnitude yielding drastic increase of the current amplitude upon the energy gap reduction ($J_c \propto 1/E_g^4$). Figure 7 and Table I present the magnitude of the circular photocurrent obtained for different samples and temperatures. Note that, to make comparison of data obtained at different frequencies possible, we used the fact that $J_c \propto 1/\omega$ and normalized the data to the radiation frequency. The figure reveals that at fixed temperature, either 300 K or 4.2 K, J_c/P substantially reduces with the band gap increase; see Table I. Furthermore, comparing the photocurrent magnitudes in each individual sample we see that the photocurrent is increased by more than two orders of magnitude at the temperature decrease from 300 to 4.2 K. This fact is in agreement with substantial reduction of the band gap at low temperatures. The values of E_g for different sample compositions x and temperatures are taken from Refs. [19,34,59]. We note that, for samples A and B at 4.2 K, the band gap becomes negative and applicability of Eq. (25) is not justified. Now we estimate from the room temperature experiment the strain $u = [\frac{2}{5}(u_{zz} - u_{yy})\frac{\sin 2\phi}{2} - u_{yz}\cos 2\phi]$. Room temperature data are used because, under these conditions, all the samples have a normal band dispersion, thus no topologically protected surface states can be formed and this case is relevant to the above derived equation for the photocurrent.

The current density j_c was obtained from the photocurrent J_c measured in the experiment after $j_c/I = J_c/P \cdot S_{\text{beam}}/(d \cdot d_{\text{beam}})$, where d is the width of the conducting channel, d_{beam} is the radiation beam diameter, and S_{beam} is the beam area.

Note that while for room temperature results this calculation seems to be reasonable at helium temperatures it is not straightforward, because free carriers and, consequently, the current may be distributed inhomogeneously across the sample. The latter unknown factor makes a quantitative comparison of 4.2 K data with the theory difficult. Table I presents the strain u obtained using the parameters $2m_0(P/\hbar)^2 = 18.8$ eV [60], $b = -1.4$ eV, and $n_\omega = 4.6$ [61]. While the ratio Ξ_{cv}/Ξ_c is unknown for HgTe, we use $\Xi_{cv}/\Xi_c = 0.3$ for GaAs [57]. Table I shows that the strain u in samples with different compositions varies from 1.6×10^{-7} to 6.9×10^{-6} and is well below the strain $u_{\max} = 1.52 \times 10^{-3}$ estimated by minimizing the elastic energy for pure HgTe ($x = 0$) deposited on the CdTe substrate [33]. We note that a small value of the strain is not surprising because we deal with thick films. Under this condition strain is expected to be z-coordinate dependent and be strongest at the bottom boundary.

We note that other possible sources of the CPGE in the films made of nongyrotropic crystals are (i) other (unrelated to strain) mechanics of bulk symmetry reduction, (ii) interface related effects, such as 2D electron states, which may occur at the interfaces or anisotropic scattering of bulk electrons at the interfaces, and (iii) topological surface states for samples with $x < x_c$. At last but not least a photocurrent sensitive to the helicity of incident photons can also emerge as a result of the circular-to-linear polarization conversion in a birefringent medium and the linear photogalvanic effect (LPGE). This scenario can be excluded since the birefringence in the THz range is very weak and such currents should be small as compared to the LPGE. In experiments, however, the circular photocurrent is even larger than the LPGE.

C. Circular photon drag effect

Finally we briefly address another mechanism of the helicity driven photocurrent which, in general, may contribute to the total photoresponse. This is the circular photon drag effect, also known as the circular dynamic Hall effect, caused by the transfer of both linear and angular momenta of radiation to free carriers. This effect was previously observed in GaAs quantum well structures [62], bulk Te crystals [63], and graphene [64,65]. Likewise the CPGE, for bulk zinc-blende crystal structure described by T_d point group this effect is

TABLE I. Experimental data for the normalized photocurrent, $j_c/I = J_c/P \cdot S_{\text{beam}}/(d \cdot d_{\text{beam}})$, carrier densities, band gaps, and the calculated strain for samples A–D at 300 K and additionally the band gap values for 4.2 K [59].

Sample	x	f (THz)	J_c/P (nA/W)	j_c/I ($\mu A/W$)	N (cm^{-3})	E_g (meV)	u (10^{-6})	E_g (meV)
			$T = 300$ K					$T = 4.2$ K
A	0.15	2.02	1.8	1.24	1.8×10^{17}	83	0.4	−32
B	0.15	2.02	1.4	1.0	1.3×10^{17}	83	0.5	−32
C	0.18	0.78	3.2	0.8	1.1×10^{17}	123	1.6	20
D	0.22	2.02	0.7	0.2	4.1×10^{16}	182	6.9	94

TABLE II. Fitting parameters J_c/P, J_0/P, J_{L1}/P, and J_{L2}/P used in Figs. 2–4 for the fits after Eq. (3).

Sample	Temperature, T(K)	Radiation frequency, f(THz)	J_c/P (nA/W)	J_0/P (nA/W)	J_{L1}/P (nA/W)	J_{L2}/P (nA/W)
A	4.2	2.54	3600	5100	−300	150
A	4.2	1.63	4500	2200	1400	260
B	4.2	2.54	74	980	13	−12
C	4.2	0.69	1200	−4200	−77	−2800
D	4.2	1.63	100	1100	208	82
A	300	2.02	1.8	7	2.3	1.3
C	300	0.78	3.2	−9.9	9	1

forbidden by symmetry. The reduction of spatial symmetry caused by lattice deformation, however, makes the effect possible. The expression for the circular drag current to first order in strain tensor components can be obtained using the theory of irreducible representations. At normal incidence of radiation in (013)-oriented structure, the circular photon drag current is given by

$$j_x^{(cpd)} = \{\alpha u_{yz} + \beta[2u_{yz}\cos 4\phi + (u_{zz} - u_{yy})\sin 4\phi]\} q P_{\rm circ} I, \tag{26}$$

where α and β are two independent constants and q is the photon wave vector.

Microscopically, the circular photon drag current emerges from the action of ac electric and magnetic fields of radiation on free carriers characterized by an anisotropic dispersion. The latter stems from the strain-induced splitting between light-hole and heavy-hole bands, described by the deformation potential b, together with the $\boldsymbol{k}\cdot\boldsymbol{p}$ coupling between the Γ_6 and Γ_8 bands. The ratio of the circular photon drag current to the CPGE can be estimated as

$$\frac{j^{(cpd)}}{j^{(cpge)}} \propto \frac{\overline{v}}{c}\frac{\tau}{\hbar/E_g}\frac{1}{\zeta}, \tag{27}$$

where $\overline{v} \approx P/\hbar$ is the characteristic electron velocity and ζ is the parameter describing the scattering asymmetry, for our microscopic model of CPGE $\zeta = \Xi_{cv}/\Xi_c = 0.3$. In our samples at room temperature the momentum relaxation time is given by $\tau \approx 50$ fs and the gap energy is given by $E_g \approx 100$ meV. For these parameters the ratio $j^{(cpd)}/j^{(cpge)} \approx 0.1$. Consequently, the contribution of the circular photon drag effect is expected to be small. We note that, in previous experiments, the circular photon drag effect was detected and studied under conditions for which the CPGE was reduced [62,64,65].

V. SUMMARY

To summarize, we demonstrate in our work the symmetry breaking in CdHgTe structures resulting in a helicity-sensitive photogalvanic current with opposite directions for excitation with right- and left-handed circularly polarized radiation. The circular photocurrent is present in films with different cadmium concentrations as well as in a wide temperature range, which supports the conclusion of the strain-induced symmetry reduction. The developed theoretical model describes the experimental data in second-order perturbation theory considering the interference of matrix elements in the probability of indirect Drude-like optical transitions involving virtual processes via intermediate states.

ACKNOWLEDGMENTS

The support from two projects of the Foundation for Polish Science: the IRAP program (Grant No. MAB/2018/9) project CENTERA, and through the TEAM project POIR.04.04.00-00-3D76/16 (TEAM/2016-3/25), the DFG, German Research Foundation, Project-ID No. 314695032–SFB 1277, the Volkswagen Stiftung Program (No. 97738), and the Program N13 of the Presidium of the RAS is gratefully acknowledged. I.Y. thanks the National Science Centre, Poland (Grant No. UMO-2017/25/N/ST3/00408) for support. G.V.B. also acknowledges support from the "BASIS" foundation.

[1] P. Capper, *Narrow-gap II-VI Compounds for Optoelectronic and Electromagnetic Applications* (Springer US, New York, 1997).
[2] P. Norton, Opto-Electron. Rev. **10**, 159 (2002).
[3] M. Henini and M. Razeghi, *Handbook of Infra-red Detection Technologies* (Elsevier Science, Amsterdam, 2002).
[4] A. Rogalski, Rep. Prog. Phys. **68**, 2267 (2005).
[5] C. Downs and T. Vandervelde, Sensors **13**, 5054 (2013).
[6] A. Rogalski, *Infrared and Terahertz Detectors, Third Edition* (Taylor & Francis Ltd., Abingdon, 2018).
[7] N. Vanamala, K. C. Santiago, and N. C. Das, AIP Adv. **9**, 025113 (2019).
[8] S. A. Dvoretsky, N. N. Mikhailov, Y. G. Sidorov, V. A. Shvets, S. N. Danilov, B. Wittman, and S. D. Ganichev, J. Electron. Mater. **39**, 918 (2010).
[9] V. V. Rumyantsev, D. V. Kozlov, S. V. Morozov, M. A. Fadeev, A. M. Kadykov, F. Teppe, V. S. Varavin, M. V. Yakushev, N. N. Mikhailov, S. A. Dvoretskii, and V. I. Gavrilenko, Semicond. Sci. Technol. **32**, 095007 (2017).
[10] S. Ruffenach, A. Kadykov, V. V. Rumyantsev, J. Torres, D. Coquillat, D. But, S. S. Krishtopenko, C. Consejo, W. Knap, S. Winnerl, M. Helm, M. A. Fadeev, N. N. Mikhailov, S. A. Dvoretskii, V. I. Gavrilenko,

S. V. Morozov, and F. Teppe, APL Mater. **5**, 035503 (2017).
[11] D. Yavorskiy, K. Karpierz, M. Baj, M. Bąk, N. Mikhailov, S. Dvoretsky, V. Gavrilenko, W. Knap, F. Teppe, and J. Usakowski, Sensors **18**, 4341 (2018).
[12] M. Bąk, D. Yavorskiy, K. Karpierz, J. Łusakowski, D. But, J. Przybytek, I. Yahniuk, G. Cywiński, W. Knap, F. Teppe, S. Krishtopenko, N. Mikhailov, S. Dvoretsky, and V. Gavrilenko, Acta Phys. Pol. A **134**, 973 (2018).
[13] J. E. Moore, Nature (London) **464**, 194 (2010).
[14] M. Z. Hasan and C. L. Kane, Rev. Mod. Phys. **82**, 3045 (2010).
[15] J. Zhang, C.-Z. Chang, Z. Zhang, J. Wen, X. Feng, K. Li, M. Liu, K. He, L. Wang, X. Chen, Q.-K. Xue, X. Ma, and Y. Wang, Nat. Commun. **2**, 574 (2011).
[16] N. N. Berchenko and M. V. Pashkovskii, Sov. Phys. Usp. **19**, 462 (1976).
[17] M. Orlita, D. M. Basko, M. S. Zholudev, F. Teppe, W. Knap, V. I. Gavrilenko, N. N. Mikhailov, S. A. Dvoretskii, P. Neugebauer, C. Faugeras, A.-L. Barra, G. Martinez, and M. Potemski, Nat. Phys. **10**, 233 (2014).
[18] J. D. Malcolm and E. J. Nicol, Phys. Rev. B **92**, 035118 (2015).
[19] F. Teppe, M. Marcinkiewicz, S. S. Krishtopenko, S. Ruffenach, C. Consejo, A. M. Kadykov, W. Desrat, D. But, W. Knap, J. Ludwig, S. Moon, D. Smirnov, M. Orlita, Z. Jiang, S. V. Morozov, V. Gavrilenko, N. N. Mikhailov, and S. A. Dvoretskii, Nat. Commun. **7**, 12576 (2016).
[20] G. Tomaka, J. Grendysa, M. Marchewka, P. Śliż, C. Becker, A. Stadler, and E. Sheregii, Opto-Electron. Rev. **25**, 188 (2017).
[21] M. I. Dyakonov and A. V. Khaetskii, JETP Lett. **33**, 110 (1981).
[22] M. Marchewka, J. Grendysa, D. Żak, G. Tomaka, P. Śliż, and E. Sheregii, Solid State Commun. **250**, 104 (2017).
[23] G. M. Minkov, A. V. Germanenko, V. A. Larionova, and O. E. Rut, Phys. Rev. B **54**, 1841 (1996).
[24] C. L. Kane and E. J. Mele, Phys. Rev. Lett. **95**, 226801 (2005).
[25] B. A. Bernevig, T. L. Hughes, and S.-C. Zhang, Science **314**, 1757 (2006).
[26] M. König, S. Wiedmann, C. Brüne, A. Roth, H. Buhmann, L. W. Molenkamp, X.-L. Qi, and S.-C. Zhang, Science **318**, 766 (2007).
[27] K. C. Nowack, E. M. Spanton, M. Baenninger, M. König, J. R. Kirtley, B. Kalisky, C. Ames, P. Leubner, C. Brüne, H. Buhmann, L. W. Molenkamp, D. Goldhaber-Gordon, and K. A. Moler, Nat. Mater. **12**, 787 (2013).
[28] K.-M. Dantscher, D. A. Kozlov, M. T. Scherr, S. Gebert, J. Bärenfänger, M. V. Durnev, S. A. Tarasenko, V. V. Bel'kov, N. N. Mikhailov, S. A. Dvoretsky, Z. D. Kvon, J. Ziegler, D. Weiss, and S. D. Ganichev, Phys. Rev. B **95**, 201103(R) (2017).
[29] C. Brüne, C. X. Liu, E. G. Novik, E. M. Hankiewicz, H. Buhmann, Y. L. Chen, X. L. Qi, Z. X. Shen, S. C. Zhang, and L. W. Molenkamp, Phys. Rev. Lett. **106**, 126803 (2011).
[30] A. M. Shuvaev, G. V. Astakhov, C. Brüne, H. Buhmann, L. W. Molenkamp, and A. Pimenov, Semicond. Sci. Technol. **27**, 124004 (2012).
[31] D. A. Kozlov, Z. D. Kvon, E. B. Olshanetsky, N. N. Mikhailov, S. A. Dvoretsky, and D. Weiss, Phys. Rev. Lett. **112**, 196801 (2014).
[32] C. Brüne, C. Thienel, M. Stuiber, J. Böttcher, H. Buhmann, E. G. Novik, C.-X. Liu, E. M. Hankiewicz, and L. W. Molenkamp, Phys. Rev. X **4**, 041045 (2014).
[33] K.-M. Dantscher, D. A. Kozlov, P. Olbrich, C. Zoth, P. Faltermeier, M. Lindner, G. V. Budkin, S. A. Tarasenko, V. V. Bel'kov, Z. D. Kvon, N. N. Mikhailov, S. A. Dvoretsky, D. Weiss, B. Jenichen, and S. D. Ganichev, Phys. Rev. B **92**, 165314 (2015).
[34] C. Rigaux, *Narrow Gap Semiconductors Physics and Applications* (Springer, Berlin, 1980), pp. 110–124.
[35] Y. Betancur-Ocampo and V. Gupta, J. Phys.: Condens. Matter **30**, 035501 (2017).
[36] S. V. Morozov, V. V. Rumyantsev, M. A. Fadeev, M. S. Zholudev, K. E. Kudryavtsev, A. V. Antonov, A. M. Kadykov, A. A. Dubinov, N. N. Mikhailov, S. A. Dvoretsky, and V. I. Gavrilenko, Appl. Phys. Lett. **111**, 192101 (2017).
[37] V. V. Utochkin, V. Y. Aleshkin, A. A. Dubinov, V. I. Gavrilenko, N. S. Kulikov, M. A. Fadeev, V. V. Rumyantsev, N. N. Mikhailov, S. A. Dvoretskii, and S. V. Morozov, Semiconductors **53**, 1154 (2019).
[38] E. L. Ivchenko, *Optical Spectroscopy of Semiconductor Nanostructures* (Alpha Sci. Int. Ltd., Harrow, 2005).
[39] S. D. Ganichev and W. Prettl, *Intense Terahertz Excitation of Semiconductors* (Oxford University Press, Oxford, 2005).
[40] Y. B. Lyanda-Geller and G. E. Pikus, Sov. Phys.-Solid State **31**, 2068 (1989).
[41] Y. G. Sidorov, S. A. Dvoretskii, V. S. Varavin, N. N. Mikhailov, M. V. Yakushev, and I. V. Sabinina, Semiconductors **35**, 1045 (2001).
[42] S.-C. Tsen, D. J. Smith, J. Hutchins, B. Skromme, Y. Chen, and S. Sivananthan, J. Cryst. Growth **159**, 58 (1996).
[43] J. P. Zanatta, P. Ferret, G. Theret, A. Million, M. Wolny, J. P. Chamonal, and G. Destefanis, J. Electron. Mater. **27**, 542 (1998).
[44] T. J. de Lyon, R. D. Rajavel, J. A. Vigil, J. E. Jensen, O. K. Wu, C. A. Cockrum, S. M. Johnson, G. M. Venzor, S. L. Bailey, I. Kasai, W. L. Ahlgren, and M. S. Smith, J. Electron. Mater. **27**, 550 (1998).
[45] S. Dvoretsky, N. Mikhailov, D. Ikusov, V. Kartashev, A. Kolesnikov, I. Sabinina, Y. G. Sidorov, and V. Shvets, in *Cadmium Telluride (CdTe) - Prospects, Challenges and Applications [Working Title]* (IntechOpen, London, 2019).
[46] P. Olbrich, J. Karch, E. L. Ivchenko, J. Kamann, B. März, M. Fehrenbacher, D. Weiss, and S. D. Ganichev, Phys. Rev. B **83**, 165320 (2011).
[47] S. D. Ganichev, U. Rössler, W. Prettl, E. L. Ivchenko, V. V. Bel'kov, R. Neumann, K. Brunner, and G. Abstreiter, Phys. Rev. B **66**, 075328 (2002).
[48] W. Weber, L. E. Golub, S. N. Danilov, J. Karch, C. Reitmaier, B. Wittmann, V. V. Bel'kov, E. L. Ivchenko, Z. D. Kvon, N. Q. Vinh, A. F. G. van der Meer, B. Murdin, and S. D. Ganichev, Phys. Rev. B **77**, 245304 (2008).
[49] C. Drexler, N. Dyakonova, P. Olbrich, J. Karch, M. Schafberger, K. Karpierz, Y. Mityagin, M. B. Lifshits, F. Teppe, O. Klimenko, Y. M. Meziani, W. Knap, and S. D. Ganichev, J. Appl. Phys. **111**, 124504 (2012).
[50] S. Ganichev, Physica B **273-274**, 737 (1999).
[51] V. V. Bel'kov, S. D. Ganichev, E. L. Ivchenko, S. A. Tarasenko, W. Weber, S. Giglberger, M. Olteanu, H. P. Tranitz, S. N. Danilov, P. Schneider, W. Wegscheider, D. Weiss, and W. Prettl, J. Phys.: Condens. Matter **17**, 3405 (2005).

[52] B. I. Sturman and V. M. Fridkin, *The Photovoltaic and Photorefractive Effects in Non-Centrosymmetric Materials* (Gordon and Breach Science Publishers, New York, 1992).

[53] Note that in samples with $x < x_c$ the CPGE caused by the optical transitions in the surface states may contribute to the total current. Formation of the topological surface states in our structures was most recently demonstrated studying the cyclotron resonance [66]. A similar current has been previously observed in HgTe 2D TIs [28] and mechanisms are overviewed in Ref. [67].

[54] S. A. Tarasenko, JETP Lett. **85**, 182 (2007).

[55] E. L. Ivchenko and S. A. Tarasenko, JETP **99**, 379 (2004).

[56] G. Bir and G. Pikus, *Symmetry and Strain-induced Effects in Semiconductors* (Wiley, New York, 1974).

[57] G. Pikus, V. Marushchak, and A. Titkov, Sov. Phys. Semicond. **22**, 115 (1988).

[58] Note that the frequency dependence of the photocurrent in Eq. (25) comes from $1/\omega$ and n_ω, while other parameters are frequency independent (for a given mechanism of scattering). In the studied frequency range the refractive index changes only slightly; therefore, frequency dependence is defined by $1/\omega$.

[59] J. P. Laurenti, J. Camassel, A. Bouhemadou, B. Toulouse, R. Legros, and A. Lusson, J. Appl. Phys. **67**, 6454 (1990).

[60] E. G. Novik, A. Pfeuffer-Jeschke, T. Jungwirth, V. Latussek, C. R. Becker, G. Landwehr, H. Buhmann, and L. W. Molenkamp, Phys. Rev. B **72**, 035321 (2005).

[61] S. Adachi, *Handbook on Physical Properties of Semiconductors* (Kluwer Academic Publishers, Boston, 2004).

[62] V. A. Shalygin, H. Diehl, C. Hoffmann, S. N. Danilov, T. Herrle, S. A. Tarasenko, D. Schuh, C. Gerl, W. Wegscheider, W. Prettl, and S. D. Ganichev, JETP Lett. **84**, 570 (2007).

[63] V. A. Shalygin, M. D. Moldavskaya, S. N. Danilov, I. I. Farbshtein, and L. E. Golub, Phys. Rev. B **93**, 045207 (2016).

[64] J. Karch, P. Olbrich, M. Schmalzbauer, C. Zoth, C. Brinsteiner, M. Fehrenbacher, U. Wurstbauer, M. M. Glazov, S. A. Tarasenko, E. L. Ivchenko, D. Weiss, J. Eroms, R. Yakimova, S. Lara-Avila, S. Kubatkin, and S. D. Ganichev, Phys. Rev. Lett. **105**, 227402 (2010).

[65] C. Jiang, V. A. Shalygin, V. Y. Panevin, S. N. Danilov, M. M. Glazov, R. Yakimova, S. Lara-Avila, S. Kubatkin, and S. D. Ganichev, Phys. Rev. B **84**, 125429 (2011).

[66] M. Otteneder, D. Sacré, I. Yahniuk, G. V. Budkin, K. Diendorfer, D. A. Kozlov, I. A. Dmitriev, N. N. Mikhailov, S. A. Dvoretsky, V. V. Bel'kov, W. Knap, and S. D. Ganichev, Phys. Status Solidi B (2020), doi:10.1002/pssb.202000023.

[67] M. V. Durnev and S. A. Tarasenko, Ann. Phys. (NY) **531**, 1800418 (2019).